JACS
JOURNAL OF THE AMERICAN CHEMICAL SOCIETY
pubs.acs.org/JACS
Article

Determinants of Ligand-Functionalized DNA Nanostructure–Cell Interactions

Glenn A. O. Cremers, Bas J. H. M. Rosier, Ab Meijs, Nicholas B. Tito, Sander M. J. van Duijnhoven, Hans van Eenennaam, Lorenzo Albertazzi, and Tom F. A. de Greef*

Cite This: J. Am. Chem. Soc. 2021, 143, 10131–10142
Read Online
ACCESS | Metrics & More | Article Recommendations | Supporting Information

ABSTRACT: Synthesis of ligand-functionalized nanomaterials with control over size, shape, and ligand orientation facilitates the design of targeted nanomedicines for therapeutic purposes. DNA nanotechnology has emerged as a powerful tool to rationally construct two- and three-dimensional nanostructures, enabling site-specific incorporation of protein ligands with control over stoichiometry and orientation. To efficiently target cell surface receptors, exploration of the parameters that modulate cellular accessibility of these nanostructures is essential. In this study, we systematically investigate tunable design parameters of antibody-functionalized DNA nanostructures binding to therapeutically relevant receptors, including the programmed cell death protein 1, the epidermal growth factor receptor, and the human epidermal growth factor receptor 2. We show that, although the native affinity of antibody-functionalized DNA nanostructures remains unaltered, the absolute number of bound surface receptors is lower compared to soluble antibodies due to receptor accessibility by the nanostructure. We explore structural determinants of this phenomenon to improve efficiency, revealing that receptor binding is mainly governed by nanostructure size and DNA handle location. The obtained results provide key insights in the ability of ligand-functionalized DNA nanostructures to bind surface receptors and yields design rules for optimal cellular targeting.

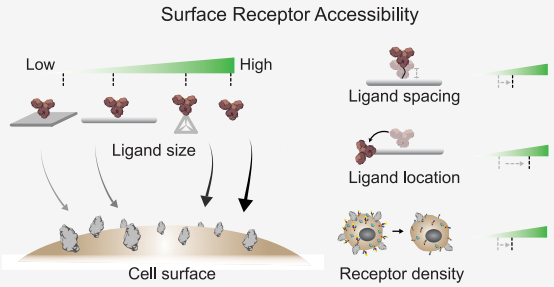

INTRODUCTION

In the last decades, nanoscale materials have emerged as a promising biomedical tool for diagnosis and treatment of diseases.[1−3] Nanomedicines are a class of nanomaterials which can be constructed from polymeric, inorganic, or organic particles containing biologically active ligands and are specifically formulated to induce cellular signaling mediated by ligand−receptor binding or to deliver therapeutic drugs to specific cells or tissues.[4,5] Incorporation of multiple ligands onto nanoparticles results in a higher avidity toward target receptors, as a result of multivalency,[6,7] and facilitates local delivery which increases drug accumulation in the site of interest, enhancing therapeutic efficiency and reducing off-target effects. Optimization of the synthesis and formulation of nanomedicines has revealed several parameters that modulate targeting efficiency and cellular uptake,[8] which include the orientation,[9] mobility,[10] and surface density of ligands on the nanoparticle.[11−13] In addition, nanoparticle size, shape, and aspect ratio also influence their uptake and therapeutic effectiveness.[14−17] For example, rod-shaped nanoparticles display more efficient cell binding compared to spherical nanoparticles,[18] whereas spherical particles more efficiently enhance cellular uptake.[19] To further unlock the potential of nanomedicines, it is crucial to control the synthesis of the nanoscale vehicles and, as such, elucidate critical design parameters for cellular targeting as a function of vehicle composition, shape, size, and geometry.

The programmability of DNA origami can be employed to construct well-defined nanostructures that allow site-specific immobilization of ligands with unprecedented control over stoichiometry and orientation.[20,21] DNA nanostructures have been used as delivery vehicles by selectively encapsulating drug molecules that can be released in a controlled fashion when the DNA nanostructure binds to specific cell types.[22,23] Additionally, these nanostructures can be used to study distance effects of receptor activation with nanometer precision[24−28] and enhance the cellular uptake of therapeutic drugs[29,30] and are able to modulate drug release kinetics.[31,32] More specifically, it has been shown that compact nanostructures with a low aspect ratio are the preferred delivery vehicles for internalization[33] and that larger DNA origami structures exhibit a higher uptake efficiency.[34] Some of the initial challenges for the use of DNA nanostructures for biomedical applications have been ad-

Received: March 1, 2021
Published: June 28, 2021

https://doi.org/10.1021/jacs.1c02298
J. Am. Chem. Soc. 2021, 143, 10131−10142

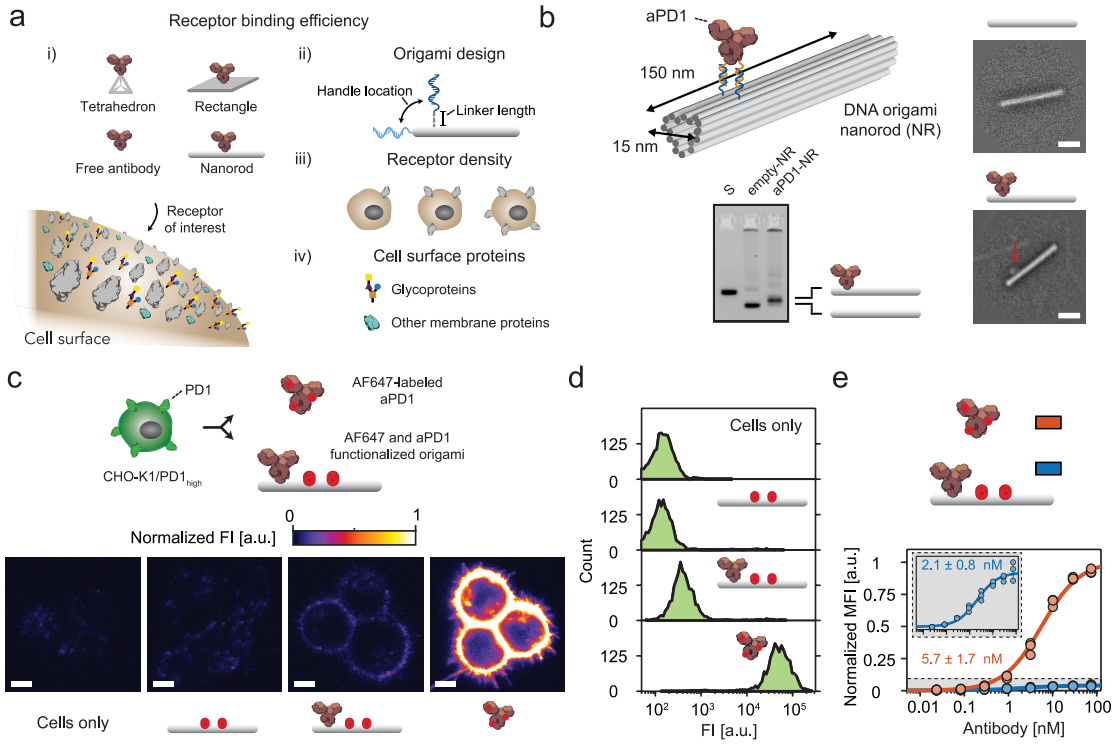

Figure 1. Targeting cellular surface receptors using antibody-functionalized DNA nanorods. (a) Schematic overview of the determinants that potentially modulate receptor binding of antibody-functionalized DNA nanostructures, including (i) DNA nanostructure size and shape, (ii) tunable DNA origami design parameters, (iii) receptor density, and (iv) the presence of other cell surface proteins. (b) Reference-free class averages obtained from single-particle TEM micrographs and electrophoretic mobility analysis of a self-assembly reaction of the 18-helix bundle nanorod with- (aPD1-NR) and without (empty-NR) the site-specific incorporation of an anti-programmed cell death protein 1 antibody (aPD1). Scale bar, 50 nm; labels: S, scaffold. (c) Confocal images and (d) flow cytometric analysis of PD1-overexpressing Chinese hamster ovary K1 (CHO-$K1_{PD1\text{-}high}$) cells incubated for 1 h with 20 nM of Alexa-647-labeled (AF647) empty-NR, aPD1-NR, or free aPD1. Scale bar, 5 μm. (e) Flow cytometric analysis of AF647-labeled aPD1 and aPD1-NR titrated to CHO-$K1_{PD1\text{-}high}$ cells for 1 h. The mean fluorescent intensities, corrected for AF67 labeling efficiency, were fitted to a noncooperative Hill equation and normalized to the fitted maximum fluorescence intensity of cells stained with AF647-aPD1 to extract the apparent dissociation constant. Individual data points represent the normalized mean fluorescent intensity (MFI) of 2000 gated single-cell events (n = 3 technical replicates).

dressed and overcome, including low-scale inefficient production, poor structural integrity in physiological fluids, and degradation by nuclease activity, making DNA origami-based nanostructures a potential platform for the design of tailored nanomedicines.[35−42]

To maximize the potential of DNA nanostructures as a generic platform for precision medicine, it is essential to analyze all parameters that influence nanostructure performance. The DNA origami method enables control over nanostructure shape, size, or ligand orientation and therefore allows the systematic investigation of a large subset of parameters that influence cellular targeting efficiency. While the parameters that modulate cellular uptake are relatively well understood, it is currently unclear if DNA nanostructures interfere with the interaction between ligands and cellular surface receptors. Although research has shown that incorporation of a protein ligand onto a DNA nanostructure does not alter the native affinity of the ligand for the receptor,[24,43] the crowded and irregularly shaped cell surface could interfere with binding of ligand-functionalized DNA nanostructures to surface receptors as a result of steric hindrance. This can lead to ineffective cellular binding of DNA nanostructure-based nanomedicines and subsequently to decreased downstream signaling efficiency and reduced therapeutic effectiveness.

In this study, we aim to systematically evaluate key parameters that modulate surface receptor binding of antibody-functionalized DNA nanostructures (Figure 1a). As a model platform, we investigate receptor binding to multiple cellular surface receptors, including programmed cell death protein 1 (PD1), epidermal growth factor receptor (EGFR), and human epidermal growth factor receptor 2 (HER2), using 18-helix bundle DNA nanorods functionalized with a single antibody.[24,43] We employ stoichiometric fluorescent labeling of antibodies to quantitatively assess cellular accessibility and show that the DNA nanorod limits the absolute number of cellular surface receptors that are bound compared to the corresponding free antibody, although the native affinity of the antibody remains unaltered. Subsequently, we use the cancer immunotherapy-related PD1 receptor[44] to study individual determinants that govern receptor accessibility in more detail. Taking advantage of the spatial addressability of DNA origami, we provide direct evidence that the DNA handle location, in contrast to linker length and electrostatic interactions, is a key parameter for optimal receptor binding. We then design multiple DNA origami structures and observe a negative correlation between receptor targeting efficiency and DNA nanostructure size. To understand the role of cellular determinants, we demonstrate that receptor accessibility is also influenced by surface receptor density and the presence of

https://doi.org/10.1021/jacs.1c02298
J. Am. Chem. Soc. 2021, 143, 10131−10142

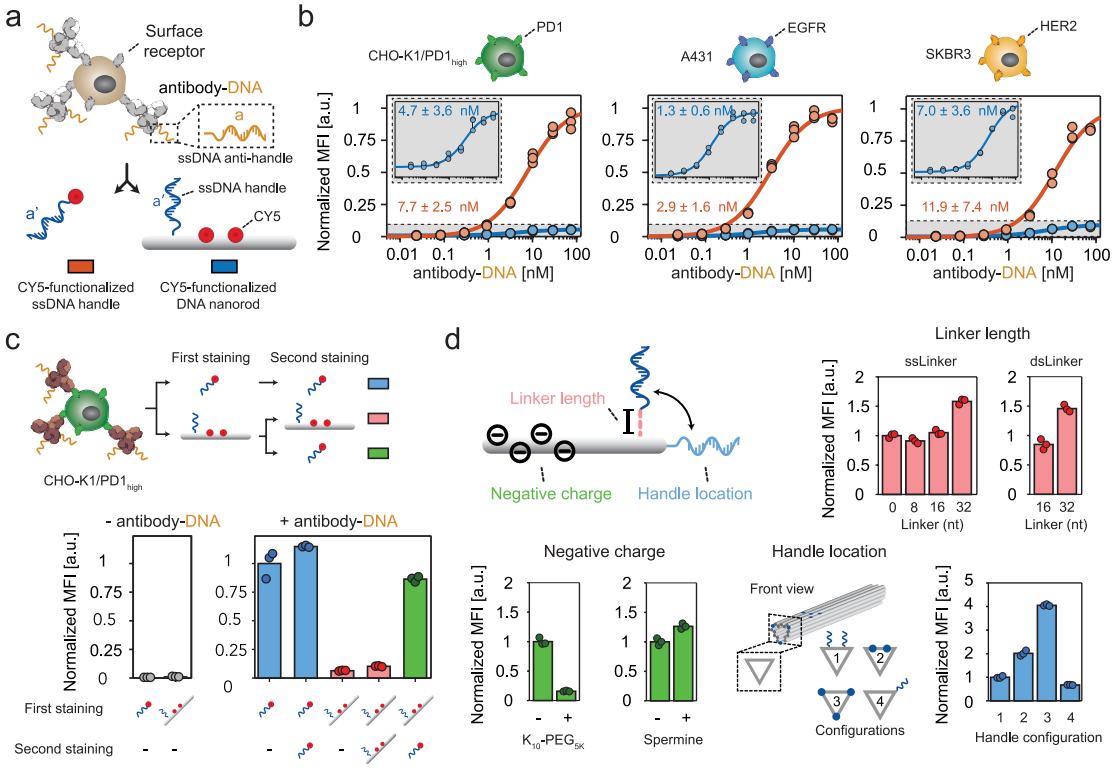

Figure 2. Quantification of DNA nanostructure-cell surface receptor interactions. (a) Schematic of the experimental setup to quantitively assess the absolute fraction of surface receptors targeted using DNA nanostructures. Twenty nM of antibodies, site-specifically labeled with 2 DNA handles, was incubated for 30 min with cells expressing target receptors and subsequently labeled with 10 nM of a complementary CY5-labeled imager strand or a CY5-functionalized DNA nanorod that includes complementary handle-extended staple strands for 30 min. (b) Flow cytometric analysis of DNA nanostructure receptor targeting in three cell lines (CHO-K1$_{PD1\text{-}high}$, A431, and SKBR3) expressing the PD1, EGFR, and HER2, respectively. Antibody-DNA conjugates (anti-PD1, Cetuximab, and Trastuzumab, respectively) were titrated to cells and subsequently labeled with CY5-functionalized imagers (CY5-IM) or CY5-functionalized nanorods (CY5-NR). The mean fluorescent intensities were fitted to a noncooperative Hill equation and normalized to the fitted MFI of cells labeled with a CY5-functionalized imager to extract the apparent dissociation constant. (c) Flow cytometric analysis of aPD1-DNA-labeled CHO-K1$_{PD1\text{-}high}$ cells that were incubated once (first staining) or twice (second staining) with only CY5-IM (blue), only CY5-NR (red), or a combination of both (green). (d) Receptor accessibility of CY5-NR as a function of tunable design parameters, including linker length (red), negative charge (green), and DNA handle location (blue). Self-assembly of all DNA nanostructures, including the K_{10}-PEG_{5K} and spermine coating, was confirmed using electrophoretic mobility analysis (Supplementary Figures 14, 17, and 19). Individual data points represent the normalized MFI of 2000 gated single-cell events (n = 3 technical replicates).

glycoproteins. Finally, we show that limited cellular accessibility of anti-PD1-functionalized DNA nanorods results in ineffective blocking of cellular PD1/PDL1 interactions *in vitro*. Taken together, our analysis provides key insights on the parameters that modulate receptor accessibility and can be used to guide the design of DNA origami nanostructures for optimal cellular targeting.

RESULTS AND DISCUSSION

Targeting Cellular Surface Receptors with Antibody-Functionalized DNA Nanorods. To investigate the role of DNA nanostructures in the interaction between ligands and cellular surface receptors, we constructed an 18-helix bundle DNA nanorod[24,31] (NR, 15 × 150 nm^2) functionalized with a single anti-PD1 antibody. We previously developed a modular conjugation strategy to site selectively couple ssDNA handles to the Fc domain of antibodies using a small photo-cross-linkable protein G adaptor that ensures correct antibody orientation on the DNA nanostructure.[43] In this work, we employed this method to site specifically conjugate two ssDNA anti-handles to the Fc region of anti-PD1 antibodies (aPD1) that hybridizes to two complementary ssDNA handles protruding from the NR surface (Supplementary Figures 1–3). Agarose gel electrophoresis confirmed the self-assembly of NRs and transmission electron microscopy revealed site-specific incorporation of DNA-aPD1 conjugates on the NR surface (Figure 1b and Supplementary Figures 4–6). Next, we used an engineered Chinese hamster ovary (CHO-K1) cell line stably expressing a high level of PD1 receptors to analyze receptor binding efficiency of AF647-labeled aPD1-NR and compare it to AF647-labeled free aPD1. We confirmed that the structural integrity of NRs was maintained during cellular labeling, while confocal microscopy analysis revealed that both aPD1-NR and free aPD1 are localized on the cellular membrane demonstrating successful binding (Figure 1c and Supplementary Figure 7). In addition, flow cytometric analysis of CHO-K1$_{PD1\text{-}high}$ cells showed an increase in mean fluorescence intensity of individual cells labeled with either aPD1-NR or free aPD1 (Figure 1d). In both measurements; however, the absolute fluorescent intensity of CHO-K1$_{PD1\text{-}high}$ cells incubated with aPD1-NR was approximately 10-fold lower than cells incubated with free aPD1. Previous research has shown that when incubated for a longer period of time, DNA origami nanostructures are readily taken up by cells.[33,34]

https://doi.org/10.1021/jacs.1c02298
J. Am. Chem. Soc. 2021, 143, 10131−10142

Since we only incubated cells over the course of 1 h with DNA nanostructures, we hypothesized that internalization only had a minor impact on the observed difference in fluorescent intensity. To fully exclude the possibility that the difference in fluorescent intensity is due to enhanced internalization of free aPD1 compared to origami-tethered aPD1, we treated aPD1-labeled cells with an acidic solution to remove cell surface aPD1.[45] Subsequently, we measured fluorescent intensity levels using flow cytometry to determine internalized fluorescent signals. The relative decrease in fluorescent intensity levels after acid treatment was similar for CHO-$K1_{PD1\text{-}high}$ cells treated with free AF647-aPD1 or AF647-labeled aPD1-NR, demonstrating that aPD1 internalization is not the primary contributor to the difference in fluorescent intensity (Supplementary Figure 8). We also tested whether the low fluorescent signal might be a result of the purification method used to remove uncoupled aPD1-DNA conjugates from functionalized aPD1-NR nanostructures. Purification of aPD1-NRs using agarose gel extraction[46] instead of two rounds of PEG precipitation, however, showed similar differences in fluorescent intensity between free AF647-aPD1 and AF647-labeled aPD1-NRs, excluding the purification method as a main source for the low levels of fluorescent intensity (Supplementary Figure 9). Collectively, these results indicate that NRs limit PD1 binding.

To assess the impact of NRs on receptor binding affinity, we titrated AF647-labeled aPD1-NR or free aPD1 against CHO-$K1_{PD1\text{-}high}$ cells and measured the mean fluorescence intensity using flow cytometry.[43,47] After correcting for AF647 labeling efficiency (Supplementary Figure 10), CHO-$K1_{PD1\text{-}high}$ labeling with free aPD1 resulted in an absolute fluorescent intensity 20-fold higher compared to aPD1-NR labeling (Figure 1e). Surprisingly, this large difference in fluorescent intensity did not translate to a different apparent dissociation constant ($K_{D,app}$) of free aPD1 and aPD1-NR, indicating that aPD1 retained its affinity when immobilized onto NRs. These experimental results were rationalized using a thermodynamic model that describes binding of antibodies to surface-tethered receptors and is able to explain the observed difference in fluorescent intensity between free aPD1 and aPD1-NR in relation to the measured the $K_{D,app}$ (Supplementary Notes and Supplementary Figure 31). Using the model, we show that $K_{D,app}$, in contrast to the absolute fluorescent intensity, is independent of the absolute number of bound receptor binding sites and only a function of the fractional occupancy of cell surface receptors. Experimentally this was verified by titrating AF647-labeled aPD1 to CHO-K1 cells expressing low, intermediate, and high levels of PD1, respectively (Supplementary Figure 11). Translating these results to the experimental data of aPD1-NR binding to CHO-$K1_{PD1\text{-}high}$ cells (Figure 1e), we therefore hypothesized that steric hindrance of NRs limits the absolute number of receptors that can bind to aPD1-NR nanostructures. Taken together, our results reveal that the native affinity of DNA origami-tethered aPD1 antibodies remains unaltered compared to free aPD1 but that the absolute number of bound DNA nanostructures is lower compared to the free antibody, resulting in a lowered binding efficiency.

Quantifying Availability of Cellular Surface Receptors to DNA Nanorods. Having shown that the DNA nanorod limits receptor binding efficiency of DNA origami-tethered aPD1 antibodies to CHO-$K1_{PD1\text{-}high}$, we sought to quantify the absolute availability of cellular receptors to DNA nanostructures. We therefore developed a general assay, using a two-step labeling method, in which we first labeled cells with DNA-antibody conjugates and subsequently incubated DNA-antibody-labeled cells with either a small CY5-functionalized imager strand (CY5-IM) or a CY5-functionalized DNA nanorod (CY5-NR) (Figure 2a). Compared to the direct labeling method used previously to determine $K_{D,app}$ (Figure 1e), this two-step labeling assay excludes the potential inhibiting effect DNA nanorods can have on antibody-receptor binding since we ensure that the interaction between the antibody and the receptor, which takes place in the first step, is not altered by the DNA nanorod. Consequently, this assay allows direct quantification of the ability of DNA nanorods to target antibody-ODN conjugates compared to a smaller imager probe and determine cellular accessibility more accurately. DNA-antibody conjugates are site-specifically functionalized with two ssDNA handles and are therefore either available to two fluorescently labeled imager strands or a single CY5-NR (Figure 1b). To establish proof of concept, we titrated DNA-aPD1 conjugates to CHO-$K1_{PD1\text{-}high}$ and fluorescently labeled the cells using a fixed concentration of imager or NR and obtained similar $K_{D,app}$ as previously determined (compare Figures 1e and 2b and Supplementary Figure 12), while the absolute fluorescent intensities showed an over 10-fold difference. Next, we evaluated receptor binding efficiency of NRs to A431 and SKBR3 cells, expressing therapeutically relevant EGFR and HER2, respectively. To this end, therapeutic antibodies Cetuximab (anti-EGFR) and Trastuzumab (anti-HER2) were conjugated to two ssDNA handles and titrated to A431 and SKBR3 cells, respectively (Supplementary Figure 13). Both experimental results similarly confirmed that receptor binding efficiency was decreased when cells were labeled with NRs, while $K_{D,app}$ remained unaltered (Figure 2b).

To exclude the possibility that the decrease in fluorescent intensity was a result of DNA-antibody or receptor dissociation, ssDNA imager internalization or DNA nanorod impurities (e.g., anti-handle excess still present after NR purification), we performed two additional control experiments. First, unlabeled CHO-$K1_{PD1\text{-}high}$ cells that were incubated with CY5-IM or CY5-NR showed similar levels of fluorescent intensity, confirming that CY5-IM and CY5-NR internalization did not impact observed differences in fluorescent intensity (Figure 2c, gray circles). Subsequently, we simultaneously assessed DNA-antibody/receptor dissociation and the influence of DNA nanorod impurities by introducing an additional washing and labeling step. In this experiment, we incubated DNA-aPD1-labeled CHO-$K1_{PD1\text{-}high}$ cells once or twice with CY5-IM or CY5-NR. Measuring the fluorescent intensity after one-step or two-step labeling did not reveal a decrease in fluorescent intensity for CHO-$K1_{PD1\text{-}high}$ cells labeled only with CY5-IM or CY5-NR, indicating no apparent dissociation of the antibody (Figure 2c, blue and red circles). Simultaneously, incubating DNA-aPD1-labeled CHO-$K1_{PD1\text{-}high}$ cells first with CY5-NR followed by CY5-IM displayed a fluorescent intensity similar to cells incubated with only CY5-IM (Figure 2c, compare blue and green circles), confirming that CY5-NR binds only a fraction of available receptor binding sites. Collectively, these results illustrate that the absolute number of cellular surface receptors targeted by DNA nanorods is limited and comprises only a small fraction of all target receptors present on the cellular surface.

Determinants of Cellular Binding Efficiency. The limited cellular binding efficiency of DNA nanorods

https://doi.org/10.1021/jacs.1c02298
J. Am. Chem. Soc. 2021, 143, 10131−10142

encouraged us to explore determinants of NR that play an important role in receptor binding. First, we focused on the high local concentration of negative charges in the DNA nanostructure caused by phosphate groups in the DNA backbone that might induce electrostatic repulsion in proximity to the negatively charged cell surface. To counteract the overall negative charge, we coated NRs with a polyethylene glycol-oligolysine copolymer which contains 10 repeats of lysines conjugated to a 5 kDa PEG molecule (K_{10}-PEG_{5K}). This method has been previously employed to prevent degradation of DNA nanostructures in low-salt conditions and protection from nucleases.[36] Coating NRs with K_{10}-PEG_{5K}, however, resulted in decreased cell surface accessibility compared to uncoated NRs (Figure 2d, green circles and Supplementary Figure 14). We hypothesized that this was a result of decreased ssDNA handle availability due to the relatively large PEG molecules on the NR surface. This was supported by additional control experiments using K_{10}-PEG_{5K}-coated aPD1-NRs which suffered less from decreased binding efficiency compared to uncoated structures (Supplementary Figure 15). Alternatively, we used spermine for NR coating; however spermine only showed little improvement in NR receptor binding (Figure 2d, green circles and Supplementary Figure 14). Since coating of NRs with polyamines could enhance cellular uptake of NRs, we additionally demonstrated that NR internalization was not improved after spermine coating (Supplementary Figure 16). Taken together, these experiments revealed that counteracting the overall negative charge had a minor impact on the binding efficiency of DNA nanorods, excluding electrostatic repulsion as a major determinant in cellular binding.

Taking advantage of the inherent programmability of DNA origami, we next assessed the influence of DNA handle length and handle location. To this end, multiple NRs were self-assembled using DNA handles that contain a 0, 8, 16 and 32-nucleotide (nt) single-stranded linker that separates the antibody from the NR surface (Supplementary Figure 17 and Table 4). Unsurprisingly, NRs that contained DNA handles with a 32-nt spacer showed the highest binding efficiency; however, the increase in cellular binding was only moderate compared to other linker lengths (Figure 2d, red circles). In addition, fortification of the 16-nt and 32-nt linker using a complementary anti-handle or, in contrast, using only a single DNA handle to improve rotational freedom for aPD1 binding did not enhance binding efficiency (Figure 2d, red circles and Supplementary Figure 18). Finally, we constructed four unique NR configurations in which the position of the ssDNA handles was varied (Figure 2d, right bottom and Supplementary Table 4). Since DNA handle incorporation efficiency strongly correlates with the position in the structure,[48] DNA handle incorporation for each configuration was quantified. Using gel mobility electrophoresis, we found that the handle incorporation efficiency of configuration 2 was lower compared to configurations 1 and 4 (Supplementary Figure 19). Rather than introducing a theoretical compensation factor to take DNA handle incorporation into account, we decided to design an additional configuration 3 similar to configuration 2 which displayed 3 instead of 2 DNA handles to compensate for the lower handle incorporation efficiency. Despite the lower incorporation efficiency, configuration 2 as well as configuration 3 showed improved cellular binding efficiency compared to configurations 1 and 4 (Figure 2d, blue circles). We attribute this improved binding efficiency to the relative orientation of NRs with respect to the cell membrane and therefore the accessibility of tethered antibodies to the cell-bound receptors.[34,49] More specifically, configurations 1 and 4 would result in lateral receptor engagement, whereas configurations 2 and 3 facilitate axial receptor binding. Additionally, to demonstrate that handle configuration only modulates absolute cellular accessibility, and, in agreement with the thermodynamic model does not translate to a change in $K_{D,app}$, we titrated DNA-aPD1 conjugates to CHO-$K1_{PD1\text{-}high}$ and fluorescently labeled the cells either using configuration 1 or configuration 3. We showed that the absolute fluorescent intensities showed over 4-fold difference, while we obtained a similar $K_{D,app}$ (Supplementary Figure 20). Collectively, these results demonstrate that receptor binding efficiency can be modulated using DNA handle location and strongly correlates with NR orientation during receptor engagement.

DNA Nanostructure Size and Shape Influence Cellular Binding Efficiency. Encouraged by the observed relation between DNA nanorod orientation and cellular binding efficiency, we constructed multiple DNA nanostructures to evaluate the effect of shape and size on receptor binding. Two additional nanostructures, a twist-corrected rectangular DNA origami rectangle[20,50] (Rec, 75 × 100 nm^2) and a tetrahedral DNA nanostructure[51] (Tet), respectively, were successfully folded and purified (Figure 3a and Supplementary Figures 21 and 22). Additionally, a 50-nt

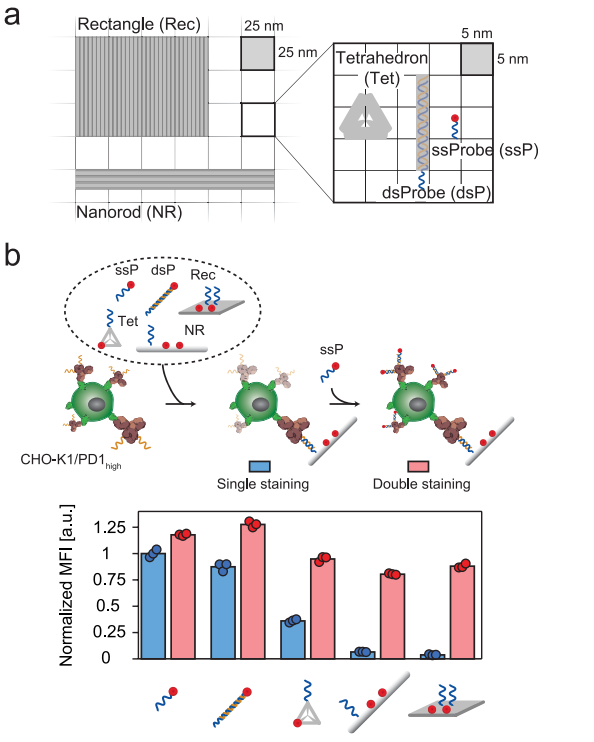

Figure 3. Effect of DNA nanostructure size and shape on receptor accessibility. (a) Schematic overview of the dimensions of different DNA nanostructures and smaller DNA probes used to target cellular surface receptors (see also Supplementary Figures 21 and 22). (b) Flow cytometric analysis of aPD1-DNA-labeled CHO-$K1_{PD1\text{-}high}$ cells first incubated with 20 nM CY5-functionalized DNA nanostructures or probes for 30 min (single staining, blue) followed by incubation with 20 nM CY5-functionalized imagers for 30 min (double staining, red). Individual data points represent the normalized MFI of 2000 gated single-cell events (n = 3 technical replicates).

https://doi.org/10.1021/jacs.1c02298
J. Am. Chem. Soc. 2021, 143, 10131−10142

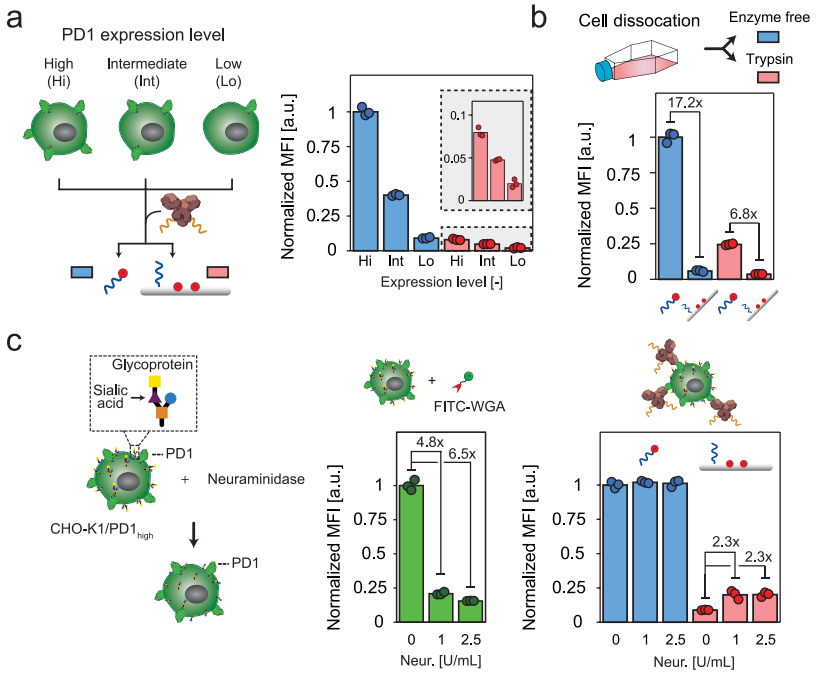

Figure 4. Effect of cellular determinants on DNA nanostructure−receptor interaction. (a) Flow cytometric analysis of CHO-K1$_{PD1\text{-}high}$ cells expressing different levels of PD1 (High, Hi; Intermediate, Int; Low, Lo). Cells were labeled with aPD1-DNA followed by incubation with CY5-functionalized imager or CY5-functionalized DNA nanorod. (b) Flow cytometric analysis of CHO-K1$_{PD1\text{-}high}$ cells that were dissociated using an enzyme-free dissociation buffer or trypsinization or (c) treated with different concentrations of neuraminidase (Neur.) to remove sialic acids. Cellular labeling was performed as described in (a). Fluorescein isothiocyanate-linked wheat germ agglutinin (FITC-WGA) was used to detect sialic acid residues. Individual data points represent the normalized MFI of 2000 gated single-cell events (n = 3 technical replicates).

double-stranded binding probe (dsP) was self-assembled. The DNA nanorod and DNA rectangle contained two ssDNA handles which facilitate binding to a single antibody (Supplementary Figure 23). In contrast, the DNA tetrahedron and double-stranded probe employed a single ssDNA handle which allows binding of two nanostructures to a single antibody, comparable to an imager strand (Figure 2a). Consequently, double-stranded binding probes and tetrahedrons are therefore labeled with a single CY5 fluorophore, while DNA rectangles and nanorods contain two CY5 labels. To accurately compare binding efficiency, CY5 fluorescent intensity of all nanostructures should be similar and scale proportionally with the number of dyes incorporated (e.g., the fluorescent intensity of the double-stranded binding probe or tetrahedron should be two times smaller than the fluorescent signal of DNA rectangles or nanorods). Using fluorescent intensity measurements and a fixed concentration of CY5-functionalized nanostructures, we demonstrated similar fluorescent intensities for CY5-IM, CY5-dsP, and CY5-Tet as well as for CY5-Rec and CY5-NR; however, it also revealed a nonproportional increase (~3-fold) in fluorescent intensity when comparing CY5-IM, CY5-dsP, or CY5-Tet to CY5-Rec and CY5-NR (Supplementary Figure 24). As a result, receptor binding efficiencies of the DNA rectangles or nanorods could be slightly overestimated when compared to the single-stranded imager, double-stranded probe, or tetrahedron. However, since the observed difference in fluorescent intensity between the large DNA nanostructures (i.e., CY5-Rec or CY5-NR) and the small DNA probe is >10-fold, we decided not to use a correction factor for this overestimation and directly rely on the fluorescent intensity observed using flow cytometric analysis. Incubating all DNA nanostructures with aPD1-DNA-labeled CHO-K1$_{PD1\text{-}high}$ cells revealed a negative correlation between nanostructure size and receptor binding efficiency. The binding efficiency of DNA rectangles, comprising a larger surface area than DNA nanorods, showed the lowest binding efficiency, indicating that aspect ratio and surface area are critical determinants of DNA nanostructure binding (Figure 3b, compare blue circles). Recovery of the fluorescent intensity after incubating labeled cells with CY5-imager strands confirmed that the decreased fluorescent intensity was a result of limited DNA nanostructure binding, rather than DNA-antibody dissociation or DNA handle impurities (Figure 3b, red circles). These results collectively demonstrate that nanostructure size negatively impacts cellular binding and suggest aspect ratio and surface area as potential parameters that modulate receptor binding efficiency.

Cellular Determinants of DNA Nanostructure Binding Efficiency. We have demonstrated that DNA nanostructure size limits cell surface accessibility and that handle location is a critical parameter to modulate receptor binding; however, all these determinants are intrinsically related to the DNA nanostructure. We therefore next investigated how cellular features, such as surface receptor density or the presence of a dense glycocalyx, impact receptor targeting efficiency of DNA nanostructures. First, we assessed the effect of PD1 density on nanostructure binding. We hypothesized that overexpression of target receptors could result in a receptor density that exceeds the theoretical number of DNA nanostructures that can bind based on surface area. Consequently, receptor binding of an individual nanostructure could block access to other surface receptors, limiting overall availability of receptor binding sites. To study this effect, we analyzed binding of CY5-IM and CY5-NR to CHO-K1 cells expressing low, intermediate, and high levels of PD1 (Figure 4a and Supplementary Figures 11 and 12). Unsurprisingly, CHO-K1 cells incubated with CY5-IM

https://doi.org/10.1021/jacs.1c02298
J. Am. Chem. Soc. 2021, 143, 10131−10142

displayed a decrease in fluorescent intensity as a function of receptor density (Figure 4a, compare blue circles). Moreover, the fluorescent intensity of CHO-K1$_{PD1\text{-}low}$ cells labeled with CY5-IM exceeds that of CHO-K1$_{PD1\text{-}high}$ cells labeled with CY5-NR. This indicates that even CHO-K1$_{PD1\text{-}low}$ cells express sufficient PD1 receptors to reach similar fluorescent intensity levels as CHO-K1$_{PD1\text{-}high}$ cells when incubated with CY5-NR. Specifically, if overexpression of target receptors significantly interferes with DNA nanostructure binding, the fluorescent intensity of CHO-K1$_{PD1\text{-}low}$ labeled with CY5-NR should be comparable to that of CY5-NR-labeled CHO-K1$_{PD1\text{-}high}$ cells. Analyzing binding of CY5-NR to CHO-K1 cells, however, displayed a decreasing trend in fluorescent intensity as a function of PD1 expression comparable to CY5-IM, providing direct evidence that PD1 density plays a minor role in DNA nanostructure binding for the investigated densities (Figure 4a, compare red circles). In addition to target receptor density, we also explored whether the presence of other surface proteins present in the crowded environment of the cell membrane could interfere with DNA nanostructure binding. To examine this, we analyzed binding of CY5-IM and CY5-NR to CHO-K1$_{PD1\text{-}high}$ cells that were dissociated using the proteolytic enzyme trypsin. Since trypsin treatment also degrades PD1 receptors present on the cell surface, this leads to an overall decrease of PD1 density which, in combination with the degradation of other cell surface, should mitigate the effect of steric hindrance. Treating cells with trypsin resulted in a 6.8-fold difference in fluorescent intensity between CY5-IM and CY5-NR compared to a 17.2-fold difference observed for untreated cells, indicating that a crowded cellular surface limits DNA nanostructure binding (Figure 4b). Taken together, these results illustrate that target receptor density in combination with a crowded cellular surface negatively impacts receptor accessibility.

Having established that receptor accessibility is sensitive to the presence of cellular surface proteins, we sought to examine the impact of the glycocalyx on DNA nanostructure binding. Previous research has shown that enzymatic digestion of the glycocalyx resulted in enhanced nanoparticle uptake.[52,53] To assess the effect of the glycocalyx on DNA nanostructure receptor binding, CHO-K1$_{PD1\text{-}high}$ cells were treated with neuraminidase to selectively remove sialic acids (Figure 4c). CHO-K1$_{PD1\text{-}high}$ cells treated with neuraminidase and incubated with CY5-IM did not exhibit improved labeling efficiency, indicating that the small imager is not affected by glycocalyx composition. In contrast, cells incubated with CY5-NR displayed a 2.3-fold increase in fluorescent intensity, confirming that the glycocalyx interferes with DNA nanostructure binding. Overall, these findings indicate that receptor targeting efficiency of DNA nanostructures is not only dependent on nanostructure design but is also significantly impacted by cell membrane properties.

aPD1-Functionalized DNA Nanorods Do Not Block Immune Checkpoint Receptors. Finally, to correlate cellular binding efficiency and modulation resultant downstream signaling, we explored how limited cellular binding efficiency of DNA nanostructures translates to receptor blocking efficiency *in vitro*. As receptor blocking efficiency is pivotal to effective immunotherapy,[44] we hypothesized that low receptor binding efficiency of aPD1-functionalized nanorods could result in a decreased checkpoint blockade and, additionally, that an optimized antibody configuration on the DNA nanorod (configuration 3, Figure 2d) could improve blocking efficiency. For these studies, we used a commercially available bioassay to measure the ability of aPD1 to block PD1/PDL1 interactions based on Jurkat T$_{PD1/TCR}$ cells reporters and CHO-K1$_{PDL1/APC}$ cells as antigen presenting cells (Figure 5a). When aPD1 antibodies were titrated to a

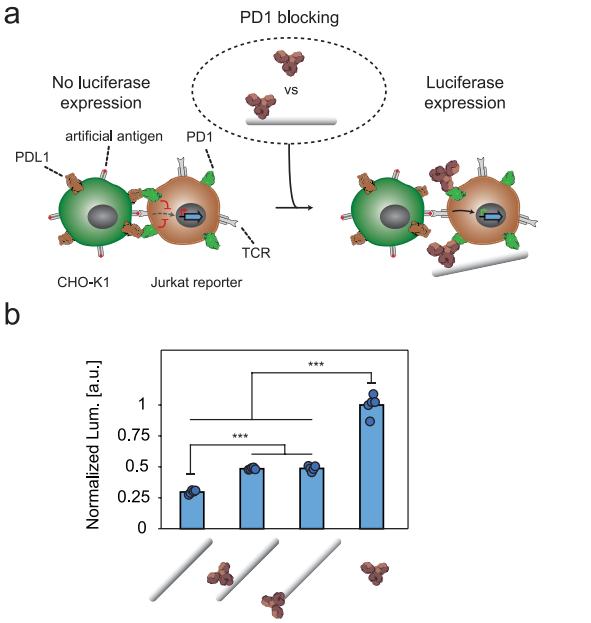

Figure 5. aPD1-functionalized DNA nanostructures are inefficient immune checkpoint inhibitors. (a) Schematic of the cell assay to detect the potency of aPD1-functionalized DNA nanorods (aPD1-NR) to block PD1/PDL1 interactions. Specifically, artificial antigen-presenting (aAPC) CHO-K1$_{PDL1/APC}$ cells that express the programmed death-ligand 1 (PDL1) were cocultured with Jurkat T$_{PD1/TCR}$ cells stably expressing PD1, T-cell receptors (TCRs), and a luciferase induced by nuclear factor of activated T cells. (b) Luciferase expression from a CHO-K1$_{PDL1/APC}$ /Jurkat T$_{PD1/TCR}$ cell coculture treated with empty-NR, aPD1-NR$_1$, aPD1-NR$_3$, and free aPD1. One-way analysis of variance was used followed by Tukey's multiple-comparison test (***P < 0.001). Individual data points represent normalized luminescence (Lum.). Experiment was performed with five technical replicates for each experiment.

coculture of Jurkat T$_{PD1/TCR}$ cells and CHO-K1$_{PDL1/APC}$, Jurkat T$_{PD1/TCR}$ cells responded in a dose-dependent manner, indicating inhibitory activity of PD1 signaling in this cell system (Supplementary Figure 25). Before assessing the blocking efficiency of aPD1-functionalized nanorods, we performed additional control experiments to validate the purity and structural integrity of DNA nanorods in culture medium. After aPD1-functionalization of DNA nanorods, we employed two rounds of PEG precipitation[43,54] or agarose gel extraction[46] to remove free aPD1 and found that only agarose gel purification resulted in full removal of free aPD1 antibodies (Supplementary Figures 26 and 27). Additionally, we confirmed the stability of aPD1-functionalized nanorods in culture medium for the duration of the blocking assay (Supplementary Figure 28). Treating a coculture of Jurkat T$_{PD1/TCR}$ cells and CHO-K1$_{PDL1/APC}$ with empty-NR, aPD1-NR$_1$, aPD1-NR$_3$, and free aPD1 revealed that free aPD1 showed a higher blocking PD1/PDL1 blocking efficiency signaling (Figure 5b). Surprisingly, no significant difference in receptor blocking efficiency was found between aPD1-NR$_1$ and aPD1-NR$_3$. Previous research has shown that next to PD1

https://doi.org/10.1021/jacs.1c02298
J. Am. Chem. Soc. 2021, 143, 10131−10142

receptor occupation level, the nanoscale spatial organization of PD1 receptors plays an important role in PD1 inhibition.[28,55,56] We therefore hypothesize that the improved cellular accessibility of aPD1-NR_3 on itself is not sufficient to improve blocking efficiency compared to aPD1-NR_1. Nevertheless, these results illustrate that inefficient cellular targeting of antibody functionalized DNA nanostructures directly translates to decreased receptor blocking efficiency *in vitro*.

CONCLUSIONS

DNA nanotechnology has facilitated the design of a library of nanostructures that have been shown to be stable in cellular environments and can be readily modified with small molecules or protein ligands to study cellular signaling at the nanoscale or act as programmable delivery vehicles.[57,58] Here, we evaluated the receptor binding efficiency of antibody-functionalized DNA nanostructures to elucidate critical design parameters that can promote or hamper cellular binding. Our results reveal that, while the native affinity of incorporated antibodies remains unaltered, the absolute number of surface receptors targeted by antibody-functionalized DNA nanostructures is reduced when compared to free antibodies. Systematic evaluation of nanostructure design parameters revealed that nanostructure orientation and size are key parameters for efficient receptor binding and demonstrated that the cell surface composition acts as a natural barrier that limits receptor accessibility. Based on these findings, we hypothesize that steric hindrance caused by the larger DNA nanostructures is the primary contributor to limited receptor binding efficiency. A potential application of this nanostructure induced steric hindrance could comprise the formation of a steric barrier around the cell that is able to block all ligand−receptor interactions. However, experimental evidence showed that the binding of large DNA nanostructures to surface receptors did not prevent other, smaller, probes from accessing unbound receptors, excluding the possibility of using large DNA nanostructures as tools for cell signaling blockage. Moreover, a cellular assay that assessed the immune checkpoint blockade displayed that decreased receptor binding efficiency of aPD1 nanostructures directly translated to limited blocking of immune checkpoint receptors. This result highlights important considerations for the use of nanostructures in biological systems and their therapeutic effectiveness. For example, smaller nanostructures containing only a limited number of therapeutic antibodies might be beneficial over larger nanostructures that contain multiple antibodies to block ligand−receptor signaling. Rationalizing the impact of individual design parameters for ligand-functionalized DNA nanostructures therefore provides a powerful addition to the design criteria for nanostructures targeting cellular surface receptors.

Aside from the absolute number of receptors that are targeted, cellular activation mechanisms also play a major role in cellular signaling. Previous work, which employed DNA nanostructures to study distance-dependent effects of receptor activation with nanometer precision, showed that ligand-functionalized DNA origami structures induced a similar or even enhanced cellular signaling compared to soluble ligands.[24,26,28,59] Combining these results with the findings in our work suggests that the number of bound ligand-functionalized DNA nanostructures compared to soluble ligands is not the only determinant that could modulate cellular signaling. Moreover, the combination of multiple ligands at the same nanoparticles has shown in the past to be advantageous to enhance selectivity by either bispecific or multivalent interactions.[47,60] Since DNA nanostructures can be programmed as drug delivery systems to display or encapsulate therapeutic molecules that are released upon binding to specific surface proteins[22,23] the results in this work provide the scientific community with guidelines to display targeting ligands at locations that are easily accessed by the cell, while at the same time incorporating therapeutic functionalities with potential side effects at locations with limited cellular accessibility.

At the same time, the role the receptor activation mechanism plays in cellular signaling underlines the limitations of using a single parameter, the equilibrium dissociation constant (K_D), to assess ligand-functionalized nanostructure performance.[61] Dissociation constants only refer to the strength of individual ligand−receptor interactions, excluding the effect of nanostructure design or cellular determinants. Our work shows that the efficacy of cellular targeting is dictated by a combination of receptor affinity and accessibility of receptors at the target site. As such, a broader subset of parameters, which include cell signaling modulation and receptor binding efficiency, should be explored to maximize the potential of nanomedicines. We envision that programmable DNA nanostructures find great application in the elucidation on critical design parameters that will eventually guide the design of precision medicines, either composed of nucleic acids, polymers, or organic molecules.

MATERIALS AND METHODS

Materials. Staple strands, handle-extended staple strands, modified DNA oligonucleotides, and fluorescently modified DNA oligonucleotides were obtained from Integrated DNA Technologies. The p7560 scaffold for the nanorod and M13mp18 scaffold for the rectangle were obtained from Eurofins. Monoclonal antibodies anti-PD1 (kindly provided by Aduro Biotech, hPD1.27.C4, batch: 18-FJ8381), Cetuximab (Erbitux, Merck), and Trastuzumab (Herceptin, Roche) were used for cell labeling.

Recombinant Protein Expression and Purification. Protein G was expressed as described previously.[62] Briefly, BL21(DE3) cells (Novagen), transformed with pet28a-protein G and pEVOL-*p*Bpf (kind provided by Peter Schultz), were grown for 18 h at 25 °C to express protein G. After lysing the cells using BugBuster (5 mL/g pellet, Merck) supplemented with benzonase (5 μL/g pellet, Merck), protein G was purified by Ni-NTA affinity chromatography followed by *Strep*-tactin chromatography, and the purity was assessed using SDS-PAGE gel analysis.

Preparation of Reaction pG-ODNs. ODN coupling was performed as previously described.[62] In a typical reaction, to a solution of 10 nmol ODN in water (10 μL) were added 1× PBS, pH 7.2 (30 μL) and 100 nmol Sulfo-SMCC (Thermo scientific) in DMSO (40 μL). The reaction was incubated at 850 rpm for 2 h at 20 °C. Excess Sulfo-SMCC was removed using two rounds of ethanol precipitation. SMCC-labeled ODNS were precipitated by the addition of 10% (v/v) 5 M NaCl and 300% (v/v) ice-cold EtOH and incubating for 75 min at −30 °C. The reaction mixture was centrifuged at 19,000×*g* for 30 min at 4 °C, the pellet was reconstituted in 1× PBS (pH 7.2), and the precipitation was repeated. After centrifugation, the pellet was washed in 95% (v/v, in water) ice-cold EtOH, centrifuged at 19,000×*g* for 15 min and lyophilized.

For conjugation of pG, to a SMCC-functionalized ODN, an aliquot of pG was buffer exchanged to (100 mM Sodium Phosphate, 25 μM TCEP, pH 7) using a PD10 desalting column (GE Healthcare). Subsequently, desalted pG was concentrated to a final concentration of 50 μM using Amicon 3 kDa MWCO centrifugal filters (Merck

https://doi.org/10.1021/jacs.1c02298
J. Am. Chem. Soc. 2021, 143, 10131−10142

Millipore). Ten nmol lyophilized SMCC-functionalized ODN was reconstituted in 40 μL 50 μM pG (2 nmol) resulting in a 5× excess of maleimide-ODN. The reaction was shaken at 850 rpm for 3 h at 20 °C.

General Procedure for pG-ODN Antibody Labeling and Purification. Protein G-ODN conjugates were coupled to an antibody as described previously.[62] Before conjugation of the antibody to the pG-ODN, all antibodies are buffer exchanged to 1× PBS (pH 7.4) using Amicon 10 kDa MWCO centrifugal filters (Merck Millipore). In a typical reaction, a 100 μL aliquot of 4 μM antibody is mixed with 40 μM of pG-ODN and exposed for 1 h to UV light (λ = 365 nm) at 4 °C. Coupled antibodies were purified using size exclusion chromatography on a Agilent 1260 Infinity system equipped with an Agilent SEC-5, 300A, 7.8 × 300 mm HPLC column. The flow rate was set to 1 mL/min using 1× PBS, pH 7.2 as a running buffer. The collected elution fractions were pooled and concentrated using a 50 kDa MWCO cutoff filter (Merck Millipore). The concentration of purified antibody−DNA conjugates was determined with gel band intensity analysis on reducing SDS-PAGE. To this end, conjugate gel band intensity of the light chain was determined using the ImageJ (v.1.52n) gel analysis plugin and then compared to a calibration curve of known concentrations of antibody.

Production of p7560 Scaffold for DNA Nanorod Design. The 7560 nt single-stranded scaffold strand was produced as described in literature.[21,63] In short, 1 μL of 100 nM ssDNA was transformed in 90 μL XL10-Gold Ultracompetent cells (Agilent) and grown overnight at 37 °C on agar plates supplemented with tetracycline (10 μg/mL, Sigma-Aldrich) according to the manufacturer's protocol. A plaque was used to inoculate 300 mL of 2xYT medium (16 g/L peptone, 5 g/L NaCl, 10 g/L yeast extract) supplemented with 5 mM $MgCl_2$, and the culture was incubated for 4 h at 37 °C. The cells were pelleted by centrifugation, and the bacteriophages were extracted from the supernatant by PEG fractionation.[63] After centrifugation, the pellet was reconstituted in TE buffer (10 mM Tris, 1 mM EDTA, pH 8.5) and lysed using buffers P2 and P3 (Qiagen). After ethanol precipitation, the single-stranded phage DNA was reconstituted in TE buffer and stored at −30 °C in DNA LoBind tubes (Eppendorf). The concentration was determined by measuring the absorption at 260 nm (ND-1000, Thermo Scientific) and the respective extinction coefficient (ssDNA 7560: 7.43 × 10^{-1} cm^{-1}).

Production and Purification of DNA Nanostructures. *DNA Nanorod.*[24] To self-assemble the 18-helix bundle nanorod 20 nM ssDNA scaffold (p7560) was mixed with 100 nM of each staple, 12 mM $MgCl_2$, 25 mM NaCl, 5 mM Tris pH 8.5, and 1 mM EDTA. Folding was carried out by rapid heat denaturation followed by slow cooling from 80 to 60 °C over the course of 20 min and a subsequent decrease from 60 to 24 °C for 14 h.

DNA Rectangle.[20,50] Folding reactions were performed in 10 mM Tris, 1 mM EDTA, 10 mM $MgCl_2$, 50 mM NaCl, pH 8.0 with 25 nM scaffold strand (M13mp18) and 250 nM of each staple strand. The reaction mixture was heated to 95 °C for 15 min and then slowly cooled to 20 °C at a rate of 1 °C/min.

Both DNA nanostructures were purified by two rounds of PEG precipitation[54] and finally dissolved in 1× PBS, pH 7.4 and 10 mM $MgCl_2$. The DNA origami concentration was determined by measuring the absorption at 260 nm and the respective extinction coefficients (DNA nanorod: 1.22 × 10^8 M^{-1} cm^{-1}, DNA rectangle: 1.24 × 10^8 M^{-1} cm^{-1}).

Tetrahedron[51] *and Double-Stranded DNA Probe.* Folding reactions were performed in 10 mM Tris, 1 mM EDTA, and 5 mM $MgCl_2$ with 1 μM of each core staple strand and 2 μM of a CY5-functionalized antihandle. The reaction mixture was heated to 95 °C for 2 min and then slowly cooled to 20 °C at a rate of 1 °C/90 s. Assembled nanostructures were analyzed and subsequently purified using native polyacrylamide gel electrophoresis (PAGE) extraction and dissolved in 5 mM Tris (pH 8.0), 0.5 mM EDTA, and 5 mM $MgCl_2$ for long-term storage or 1× PBS, pH 7.4 and 10 mM $MgCl_2$ for immediate use. The concentration was determined by measuring the absorption at 260 nm and the respective extinction coefficients (DNA tetrahedron: 2.66 × 10^6 M^{-1} cm^{-1}, DNA double-stranded probe: 1.06 × 10^6 M^{-1} cm^{-1}).

Antibody-Nanorod Production and Purification. Incorporation of DNA-labeled antibodies onto purified DNA origami nanostructures was performed by incubating DNA origami with 4 mol equiv of antibody-DNA for 1 h at 37 °C, followed by 2h at 22 °C in 1× PBS, pH 7.4 and 10 mM $MgCl_2$. Removal of excess antibody-DNA was carried out either using two rounds of PEG precipitation as described before[43] (Figure 1) or using 1.5% agarose gel extraction[64] (Figure 5). Antibody incorporation efficiency was quantified using 1.5% agarose gel electrophoresis in combination with gel band intensity analysis performed using ImageJ (NIH).

Transmission Electron Microscopy. The 2.5 nM DNA nanorods were adsorbed for 1 min onto grids (Cressington 206Carbon) that were surface plasma treated for 40 s. Subsequently, the grids were stained with a 0.4% (w/v) aqueous uranyl acetate solution, and excess sample was immediately removed with filter paper. Imaging was performed at 25,000× and 29,000× magnification with a Tecnai 200 kV D2029 Twin microscope using transmission electron microscopy (TEM) uP SA Zoom mode, and images were captured at 4096 × 4096 pixels with 4.27 Å/pixel and 3.59 Å/pixel, respectively. The nanoparticles were individually picked (∼20 per nanostructure) from micrographs with the boxer function in EMAN2.3.[65] Two-dimensional class averages were constructed with the bispectrum-based class averaging function from EMAN2.3 and classified into two classes based on mean intensity.

Fluorescent Antibody Labeling. Antibodies were buffer exchanged to 100 mM sodium phosphate buffer (pH 7.0) using Zeba spin desalting columns, 7K MWCO (Thermofisher). Alexafluor647 (AF647) NHS ester (Thermofisher) was added in a 20-fold molar excess and reacted for 2 h at room temperature. Subsequently, nonreacted dye was removed using Zeba spin desalting columns, 7K MWCO. The labeling efficiency was based on the absorbance at 280 and 647 nm and assuming extinction coefficients of 210,000 M^{-1} cm^{-1} and 270,000 M^{-1} cm^{-1} for the antibody and AF647, respectively. In addition, the contamination of free dye was quantified using SDS-PAGE gel analysis.

Cell Culture. Monoclonal CHO-K1 cells stably expressing low, intermediate, and high levels of PD1 (kindly provided by Aduro Biotech) were cultured in a 75 cm^2 flask in Dulbecco's modified Eagle/F12 (DMEM/F12) medium (cat: 11320033) supplemented with 5% fetal bovine serum (FBS) (cat: 26140079), 1% penicillin-steptomycin (P/S) (cat: 15140122), and 0.8 mg/mL geneticin sulfate (G418) (cat: sc-29065A). A431 cells (ATCC, cat. no. CRL-1555) and SKBR3 cells (ATCC, cat. no. HTB-30) overexpressing EGFR and HER2, respectively, were cultured in RPMI1640 medium (cat: 11875093) supplemented with 10% FBS and 1% P/S. For the SKBR3 cells, the culture medium was supplemented with 1 mM sodium pyruvate (cat. 11360070). Cells were incubated at 37 °C with 5% CO_2.

Fluorescent Cellular Labeling. Unless stated otherwise, CHO-K1 cells were harvested using enzyme-free cell dissociation buffer (cat: 13151014) and A431/SKBR3 cells using trypsin/EDTA (0.05%) (cat: 25300062). Cells were washed in labeling buffer (1× PBS, 0.1% BSA (w/v), pH 7.4) and diluted to a final concentration of 3.5 × 10^6 cells/mL in labeling buffer.

One-step Labeling Using anti-PD1-Functionalized DNA Nanorod (Figure 1). 2.86 μL of the cell suspension (10,000 cells) was incubated in a final volume of 20 μL of labeling buffer containing 20 nM aPD1-Nanorod-AF647 or 20 nM aPD1-AF647. The reaction mixture was shaken at 400 rpm for 60 min at room temperature. Subsequently, the labeled cells were centrifuged for 5 min at 1500×*g*, and the supernatant was removed. Directly prior to flow cytometry or confocal microscopy cells were resuspended in 200 μL of labeling buffer.

Two-Step Labeling Using DNA-Functionalized Antibodies (Figures 2−4). 4.29 μL of the cell suspension (15,000 cells) was incubated in a final volume of 30 μL of labeling buffer containing 20 nM DNA-antibody conjugate. The reaction mixture was shaken at 400 rpm for 30 min at room temperature. Subsequently, the labeled

https://doi.org/10.1021/jacs.1c02298
J. Am. Chem. Soc. 2021, 143, 10131−10142

cells were centrifuged for 5 min at 1500×*g*, and the supernatant was removed. The pelleted cells were redissolved in 30 μL of labeling buffer containing 10 nM complementary CY5-labeled imager strands or CY5-functionalized DNA nanorods that include a complementary handle-extended staple strand and incubated at 400 rpm for 30 min at room temperature. The labeled cells were centrifuged for 5 min at 1500×*g*, and the supernatant was removed. Directly prior to flow cytometry, cells were resuspended in 200 μL of labeling buffer.

Confocal microscopy was performed on a Zeiss LSM510 META NLO equipped with a C-Apochromat 63×/1.2W objective using a 633 nm He/Ne laser. The pinhole was set to 1 airy unit, and images of 2048 × 2048 pixels were acquired with a pixel dwell of 3.2 μs. Flow cytometry was performed on a FACS Aria III (BD Biosciences) equipped with a 70 μm nozzle. Events representing single cells were gated based on the forward height scatter vs the forward area scatter. For each measurement, fluorescence intensities of 2000 individual cells were recorded and analyzed using custom-written MATLAB scripts.

Spermine and K_{10}-PEG_{5K} Coating. Spermine and K_{10}-PEG_{5K} were dissolved in Milli-Q at a final concentration of 10 mM and 1 mM, respectively. Subsequently, DNA nanostructure coating was performed for 30 min at 20 °C using N:P ratios of 10 (spermine) or 2.5 (K_{10}-PEG_{5K}), respectively.

Neuraminidase Treatment Cells. Neuraminidase from *Clostridium perfringens* (Sigma) was dissolved in 1× PBS, pH 7.4 at a final concentration of 10 U/mL. For neuraminidase treatment CHO-$K1_{PD1\text{-}high}$ cells were harvested using enzyme free cell dissociation buffer and were resuspended in DMEM/F12 medium without FBS, P/S and G418. Neuraminidase treatment was performed in a total volume of 150 μL with a cell concentration of 1×10^6 cells for 1h at 37 °C. After incubation cells were centrifuged for 3 min at 1500×*g* and washed 1 time in labeling buffer. Subsequently, cells were labeled using FITC-labeled lectin from *Triticum vulgaris* (Sigma) at a concentration of 100 μg/mL for 30 min at 20 °C. The labeled cells were centrifuged for 5 min at 1500×*g*, and the supernatant was removed. Directly prior to flow cytometry or confocal microscopy, cells were resuspended in 200 μL of labeling buffer.

PD1/PD-L1 Blocking Assay. The PD1/PD-L1 blocking assay was obtained from Promega (J1255) and was performed according to the manufacturer's instructions. Briefly, a sterile 384-well plate (Thermo Scientific, cat. 164610) was seeded with 25 μL of diluted PD-L1 aAPC/CHO-K1 thaw-and-use cells (500,000 cells/mL) and incubated at 37 °C with 5% CO_2 for 18 h. After incubation, the 384-well plate was inverted to remove the culture medium, and cells were directly incubated with 10 μL of 20 nM IgG, empty-NR, aPD-NR, or aPD1 in RPMI1640 supplemented with 1% FBS. Subsequently, 10 μL of diluted PD1 Jurkat T effector thaw-and-use cells (900,000 cells/mL) was added to the same well to yield a final concentration of 10 nM IgG, empty-NR, aPD-NR, or aPD1. Cells were incubated at 37 °C with 5% CO_2 for 6 h, and luciferase expression was quantified by adding 20 μL of Bio-Glo reagent. Luminescence was measured in a Tecan Spark 10 M platereader.

■ ASSOCIATED CONTENT

Supporting Information

The Supporting Information is available free of charge at https://pubs.acs.org/doi/10.1021/jacs.1c02298.

Extensive experimental methods and supplemental figures of DNA origami synthesis, purification, characterization, and additional cell-binding experiments (PDF)

■ AUTHOR INFORMATION

Corresponding Author

Tom F. A. de Greef − *Laboratory of Chemical Biology and Institute for Complex Molecular Systems and Computational Biology Group, Department of Biomedical Engineering, Eindhoven University of Technology, 5600 MB Eindhoven, The Netherlands; Institute for Molecules and Materials, Radboud University, 6525 AJ Nijmegen, The Netherlands; Center for Living Technologies, Eindhoven-Wageningen-Utrecht Alliance, 5600 MB Eindhoven, The Netherlands;* Email: t.f.a.d.greef@tue.nl

Authors

Glenn A. O. Cremers − *Laboratory of Chemical Biology and Institute for Complex Molecular Systems and Computational Biology Group, Department of Biomedical Engineering, Eindhoven University of Technology, 5600 MB Eindhoven, The Netherlands*

Bas J. H. M. Rosier − *Laboratory of Chemical Biology and Institute for Complex Molecular Systems and Computational Biology Group, Department of Biomedical Engineering, Eindhoven University of Technology, 5600 MB Eindhoven, The Netherlands;* orcid.org/0000-0002-0062-7087

Ab Meijs − *Laboratory of Chemical Biology and Institute for Complex Molecular Systems and Computational Biology Group, Department of Biomedical Engineering, Eindhoven University of Technology, 5600 MB Eindhoven, The Netherlands; Department of Biosystems Science and Engineering, ETH Zurich, 4058 Basel, Switzerland*

Nicholas B. Tito − *Electric Ant Lab, 1098 XG Amsterdam, The Netherlands;* orcid.org/0000-0002-8602-012X

Sander M. J. van Duijnhoven − *Aduro Biotech Europe B.V., 5349 AB Oss, The Netherlands*

Hans van Eenennaam − *Aduro Biotech Europe B.V., 5349 AB Oss, The Netherlands*

Lorenzo Albertazzi − *Laboratory of Chemical Biology and Institute for Complex Molecular Systems and Molecular Biosensing for Medical Diagnostics, Department of Biomedical Engineering, Eindhoven University of Technology, 5600 MB Eindhoven, The Netherlands;* orcid.org/0000-0002-6837-0812

Complete contact information is available at: https://pubs.acs.org/10.1021/jacs.1c02298

Notes

The authors declare no competing financial interest.

■ ACKNOWLEDGMENTS

We thank J. Schill for help with the TEM imaging and analysis. M. Merkx, P. de Vink, and D. Schrijver are gratefully acknowledged for valuable insights and fruitful discussions. We thank Promega for making it possible to provide the PD1/PDL1 Blockade Bioassay cells. This work was supported by the European Research Council (ERC) (project no. 677313 BioCircuit), an NWO-VIDI grant from The Netherlands Organization for Scientific Research (NWO, 723.016.003), and funding from the Ministry of Education, Culture and Science (Gravity programs, 024.001.035 and 024.003.013).

■ REFERENCES

(1) Doshi, N.; Mitragotri, S. Designer Biomaterials for Nanomedicine. *Adv. Funct. Mater.* **2009**, *19* (24), 3843−3854.

(2) Howes, P. D.; Chandrawati, R.; Stevens, M. M. Colloidal Nanoparticles as Advanced Biological Sensors. *Science* **2014**, *346* (6205), 1247390.

(3) Mitragotri, S.; Anderson, D. G.; Chen, X.; Chow, E. K.; Ho, D.; Kabanov, A. V.; Karp, J. M.; Kataoka, K.; Mirkin, C. A.; Petrosko, S. H.; Shi, J.; Stevens, M. M.; Sun, S.; Teoh, S.; Venkatraman, S. S.; Xia,

Y.; Wang, S.; Gu, Z.; Xu, C. Accelerating the Translation of Nanomaterials in Biomedicine. *ACS Nano* **2015**, *9* (7), 6644−6654.
(4) Tran, S.; DeGiovanni, P.-J.; Piel, B.; Rai, P. Cancer Nanomedicine: A Review of Recent Success in Drug Delivery. *Clin. Transl. Med.* **2017**, *6* (1), e44 DOI: 10.1186/s40169-017-0175-0.
(5) Liu, Z.; Jiang, W.; Nam, J.; Moon, J. J.; Kim, B. Y. S. Immunomodulating Nanomedicine for Cancer Therapy. *Nano Lett.* **2018**, *18* (11), 6655−6659.
(6) Simnick, A. J.; Valencia, C. A.; Liu, R.; Chilkoti, A. Morphing Low-Affinity Ligands into High-Avidity Nanoparticles by Thermally Triggered Self-Assembly of a Genetically Encoded Polymer. *ACS Nano* **2010**, *4* (4), 2217−2227.
(7) Martinez-Veracoechea, F. J.; Frenkel, D. Designing Super Selectivity in Multivalent Nano-Particle Binding. *Proc. Natl. Acad. Sci. U. S. A.* **2011**, *108* (27), 10963−10968.
(8) Tian, X.; Angioletti-Uberti, S.; Battaglia, G. On the Design of Precision Nanomedicines. *Sci. Adv.* **2020**, *6*, eaat0919.
(9) Yong, K. W.; Yuen, D.; Chen, M. Z.; Porter, C. J. H.; Johnston, A. P. R. Pointing in the Right Direction: Controlling the Orientation of Proteins on Nanoparticles Improves Targeting Efficiency. *Nano Lett.* **2019**, *19* (3), 1827−1831.
(10) Yong, K. W.; Yuen, D.; Chen, M. Z.; Johnston, A. P. R. Engineering the Orientation, Density, and Flexibility of Single-Domain Antibodies on Nanoparticles To Improve Cell Targeting. *ACS Appl. Mater. Interfaces* **2020**, *12* (5), 5593−5600.
(11) Johnston, A. P. R.; Kamphuis, M. M. J.; Such, G. K.; Scott, A. M.; Nice, E. C.; Heath, J. K.; Caruso, F. Targeting Cancer Cells: Controlling the Binding and Internalization of Antibody-Functionalized Capsules. *ACS Nano* **2012**, *6* (8), 6667−6674.
(12) Colombo, M.; Fiandra, L.; Alessio, G.; Mazzucchelli, S.; Nebuloni, M.; De Palma, C.; Kantner, K.; Pelaz, B.; Rotem, R.; Corsi, F.; Parak, W. J.; Prosperi, D. Tumour Homing and Therapeutic Effect of Colloidal Nanoparticles Depend on the Number of Attached Antibodies. *Nat. Commun.* **2016**, *7* (1), 13818.
(13) Zhang, Q.; Reinhard, B. M. Ligand Density and Nanoparticle Clustering Cooperate in the Multivalent Amplification of Epidermal Growth Factor Receptor Activation. *ACS Nano* **2018**, *12* (10), 10473−10485.
(14) Wang, J.; Byrne, J. D.; Napier, M. E.; DeSimone, J. M. More Effective Nanomedicines through Particle Design. *Small* **2011**, *7* (14), 1919−1931.
(15) Shimoni, O.; Yan, Y.; Wang, Y.; Caruso, F. Shape-Dependent Cellular Processing of Polyelectrolyte Capsules. *ACS Nano* **2013**, *7* (1), 522−530.
(16) Dasgupta, S.; Auth, T.; Gompper, G. Shape and Orientation Matter for the Cellular Uptake of Nonspherical Particles. *Nano Lett.* **2014**, *14* (2), 687−693.
(17) Shang, L.; Nienhaus, K.; Nienhaus, G. Engineered Nanoparticles Interacting with Cells: Size Matters. *J. Nanobiotechnol.* **2014**, *12* (1), 5.
(18) Barua, S.; Yoo, J.-W.; Kolhar, P.; Wakankar, A.; Gokarn, Y. R.; Mitragotri, S. Particle Shape Enhances Specificity of Antibody-Displaying Nanoparticles. *Proc. Natl. Acad. Sci. U. S. A.* **2013**, *110* (9), 3270−3275.
(19) Chithrani, B. D.; Ghazani, A. A.; Chan, W. C. W. Determining the Size and Shape Dependence of Gold Nanoparticle Uptake into Mammalian Cells. *Nano Lett.* **2006**, *6* (4), 662−668.
(20) Rothemund, P. W. K. Folding DNA to Create Nanoscale Shapes and Patterns. *Nature* **2006**, *440* (7082), 297−302.
(21) Douglas, S. M.; Dietz, H.; Liedl, T.; Högberg, B.; Graf, F.; Shih, W. M. Self-Assembly of DNA into Nanoscale Three-Dimensional Shapes. *Nature* **2009**, *459* (7245), 414−418.
(22) Douglas, S. M.; Bachelet, I.; Church, G. M. A Logic-Gated Nanorobot for Targeted Transport of Molecular Payloads. *Science* **2012**, *335* (6070), 831−834.
(23) Li, S.; Jiang, Q.; Liu, S.; Zhang, Y.; Tian, Y.; Song, C.; Wang, J.; Zou, Y.; Anderson, G. J.; Han, J.-Y.; Chang, Y.; Liu, Y.; Zhang, C.; Chen, L.; Zhou, G.; Nie, G.; Yan, H.; Ding, B.; Zhao, Y. A DNA Nanorobot Functions as a Cancer Therapeutic in Response to a Molecular Trigger in Vivo. *Nat. Biotechnol.* **2018**, *36* (3), 258−264.
(24) Shaw, A.; Lundin, V.; Petrova, E.; Fördös, F.; Benson, E.; Al-Amin, A.; Herland, A.; Blokzijl, A.; Högberg, B.; Teixeira, A. I. Spatial Control of Membrane Receptor Function Using Ligand Nanocalipers. *Nat. Methods* **2014**, *11* (8), 841−846.
(25) Kwon, P. S.; Ren, S.; Kwon, S.-J.; Kizer, M. E.; Kuo, L.; Xie, M.; Zhu, D.; Zhou, F.; Zhang, F.; Kim, D.; Fraser, K.; Kramer, L. D.; Seeman, N. C.; Dordick, J. S.; Linhardt, R. J.; Chao, J.; Wang, X. Designer DNA Architecture Offers Precise and Multivalent Spatial Pattern-Recognition for Viral Sensing and Inhibition. *Nat. Chem.* **2020**, *12*, 26.
(26) Veneziano, R.; Moyer, T. J.; Stone, M. B.; Wamhoff, E.-C.; Read, B. J.; Mukherjee, S.; Shepherd, T. R.; Das, J.; Schief, W. R.; Irvine, D. J.; Bathe, M. Role of Nanoscale Antigen Organization on B-Cell Activation Probed Using DNA Origami. *Nat. Nanotechnol.* **2020**, *15* (8), 716−723.
(27) Liu, S.; Jiang, Q.; Zhao, X.; Zhao, R.; Wang, Y.; Wang, Y.; Liu, J.; Shang, Y.; Zhao, S.; Wu, T.; Zhang, Y.; Nie, G.; Ding, B. A DNA Nanodevice-Based Vaccine for Cancer Immunotherapy. *Nat. Mater.* **2021**, *20* (3), 421−430.
(28) Fang, T.; Alvelid, J.; Spratt, J.; Ambrosetti, E.; Testa, I.; Teixeira, A. I. Spatial Regulation of T-Cell Signaling by Programmed Death-Ligand 1 on Wireframe DNA Origami Flat Sheets. *ACS Nano* **2021**, *15* (2), 3441−3452.
(29) Jiang, Q.; Song, C.; Nangreave, J.; Liu, X.; Lin, L.; Qiu, D.; Wang, Z.-G.; Zou, G.; Liang, X.; Yan, H.; Ding, B. DNA Origami as a Carrier for Circumvention of Drug Resistance. *J. Am. Chem. Soc.* **2012**, *134* (32), 13396−13403.
(30) Zhang, Q.; Jiang, Q.; Li, N.; Dai, L.; Liu, Q.; Song, L.; Wang, J.; Li, Y.; Tian, J.; Ding, B.; Du, Y. DNA Origami as an *In Vivo* Drug Delivery Vehicle for Cancer Therapy. *ACS Nano* **2014**, *8* (7), 6633−6643.
(31) Zhao, Y.-X.; Shaw, A.; Zeng, X.; Benson, E.; Nyström, A. M.; Högberg, B. DNA Origami Delivery System for Cancer Therapy with Tunable Release Properties. *ACS Nano* **2012**, *6* (10), 8684−8691.
(32) Ranallo, S.; Sorrentino, D.; Ricci, F. Orthogonal Regulation of DNA Nanostructure Self-Assembly and Disassembly Using Antibodies. *Nat. Commun.* **2019**, *10* (1), 5509.
(33) Bastings, M. M. C.; Anastassacos, F. M.; Ponnuswamy, N.; Leifer, F. G.; Cuneo, G.; Lin, C.; Ingber, D. E.; Ryu, J. H.; Shih, W. M. Modulation of the Cellular Uptake of DNA Origami through Control over Mass and Shape. *Nano Lett.* **2018**, *18* (6), 3557−3564.
(34) Wang, P.; Rahman, M. A.; Zhao, Z.; Weiss, K.; Zhang, C.; Chen, Z.; Hurwitz, S. J.; Chen, Z. G.; Shin, D. M.; Ke, Y. Visualization of the Cellular Uptake and Trafficking of DNA Origami Nanostructures in Cancer Cells. *J. Am. Chem. Soc.* **2018**, *140* (7), 2478−2484.
(35) Shaw, A.; Benson, E.; Högberg, B. Purification of Functionalized DNA Origami Nanostructures. *ACS Nano* **2015**, *9* (5), 4968−4975.
(36) Ponnuswamy, N.; Bastings, M. M. C.; Nathwani, B.; Ryu, J. H.; Chou, L. Y. T.; Vinther, M.; Li, W. A.; Anastassacos, F. M.; Mooney, D. J.; Shih, W. M. Oligolysine-Based Coating Protects DNA Nanostructures from Low-Salt Denaturation and Nuclease Degradation. *Nat. Commun.* **2017**, *8*, 15654.
(37) Praetorius, F.; Kick, B.; Behler, K. L.; Honemann, M. N.; Weuster-Botz, D.; Dietz, H. Biotechnological Mass Production of DNA Origami. *Nature* **2017**, *552* (7683), 84−87.
(38) Anastassacos, F. M.; Zhao, Z.; Zeng, Y.; Shih, W. M. Glutaraldehyde Cross-Linking of Oligolysines Coating DNA Origami Greatly Reduces Susceptibility to Nuclease Degradation. *J. Am. Chem. Soc.* **2020**, *142* (7), 3311−3315.
(39) Hahn, J.; Wickham, S. F. J.; Shih, W. M.; Perrault, S. D. Addressing the Instability of DNA Nanostructures in Tissue Culture. *ACS Nano* **2014**, *8* (9), 8765−8775.
(40) Gerling, T.; Kube, M.; Kick, B.; Dietz, H. Sequence-Programmable Covalent Bonding of Designed DNA Assemblies. *Sci. Adv.* **2018**, *4*, eaau1157.

(41) Wang, S.-T.; Gray, M. A.; Xuan, S.; Lin, Y.; Byrnes, J.; Nguyen, A. I.; Todorova, N.; Stevens, M. M.; Bertozzi, C. R.; Zuckermann, R. N.; Gang, O. DNA Origami Protection and Molecular Interfacing through Engineered Sequence-Defined Peptoids. *Proc. Natl. Acad. Sci. U. S. A.* **2020**, *117* (12), 6339−6348.
(42) Yeldell, S. B.; Seitz, O. Nucleic Acid Constructs for the Interrogation of Multivalent Protein Interactions. *Chem. Soc. Rev.* **2020**, *49* (19), 6848−6865.
(43) Rosier, B. J. H. M.; Cremers, G. A. O.; Engelen, W.; Merkx, M.; Brunsveld, L.; de Greef, T. F. A. Incorporation of Native Antibodies and Fc-Fusion Proteins on DNA Nanostructures via a Modular Conjugation Strategy. *Chem. Commun.* **2017**, *53* (53), 7393−7396.
(44) Mellman, I.; Coukos, G.; Dranoff, G. Cancer Immunotherapy Comes of Age. *Nature* **2011**, *480* (7378), 480−489.
(45) Arlauckas, S. P.; Garris, C. S.; Kohler, R. H.; Kitaoka, M.; Cuccarese, M. F.; Yang, K. S.; Miller, M. A.; Carlson, J. C.; Freeman, G. J.; Anthony, R. M.; et al. In Vivo Imaging Reveals a Tumor-Associated Macrophage-Mediated Resistance Pathway in Anti-PD-1 Therapy. *Sci. Transl. Med.* **2017**, *9* (389), eaal3604.
(46) Bellot, G.; McClintock, M. A.; Lin, C.; Shih, W. M. Recovery of Intact DNA Nanostructures after Agarose Gel-Based Separation. *Nat. Methods* **2011**, *8* (3), 192−194.
(47) Csizmar, C. M.; Petersburg, J.; Perry, T. J.; Rozumalski, L.; Hackel, B. J.; Wagner, C. R. Multivalent Ligand Binding to Cell Membrane Antigens: Defining the Interplay of Affinity, Valency, and Expression Density. *J. Am. Chem. Soc.* **2019**, *141*, 251.
(48) Strauss, M. T.; Schueder, F.; Haas, D.; Nickels, P. C.; Jungmann, R. Quantifying Absolute Addressability in DNA Origami with Molecular Resolution. *Nat. Commun.* **2018**, *9* (1), 1600 DOI: 10.1038/s41467-018-04031-z.
(49) Liu, Y.; Wijesekara, P.; Kumar, S.; Wang, W.; Ren, X.; Taylor, R. E. The Effects of Overhang Placement and Multivalency on Cell Labeling by DNA Origami. *Nanoscale* **2021**, *13* (14), 6819−6828.
(50) Rosier, B. J. H. M.; Markvoort, A. J.; Gumí Audenis, B.; Roodhuizen, J. A. L.; den Hamer, A.; Brunsveld, L.; de Greef, T. F. A. Proximity-Induced Caspase-9 Activation on a DNA Origami-Based Synthetic Apoptosome. *Nat. Catal.* **2020**, *3* (3), 295−306.
(51) Sundah, N. R.; Ho, N. R. Y.; Lim, G. S.; Natalia, A.; Ding, X.; Liu, Y.; Seet, J. E.; Chan, C. W.; Loh, T. P.; Shao, H. Barcoded DNA Nanostructures for the Multiplexed Profiling of Subcellular Protein Distribution. *Nat. Biomed. Eng.* **2019**, *3* (9), 684−694.
(52) Atukorale, P. U.; Yang, Y.-S.; Bekdemir, A.; Carney, R. P.; Silva, P. J.; Watson, N.; Stellacci, F.; Irvine, D. J. Influence of the Glycocalyx and Plasma Membrane Composition on Amphiphilic Gold Nanoparticle Association with Erythrocytes. *Nanoscale* **2015**, *7* (26), 11420−11432.
(53) Möckl, L.; Hirn, S.; Torrano, A. A.; Uhl, B.; Bräuchle, C.; Krombach, F. The Glycocalyx Regulates the Uptake of Nanoparticles by Human Endothelial Cells *in Vitro*. *Nanomedicine* **2017**, *12* (3), 207−217.
(54) Stahl, E.; Martin, T. G.; Praetorius, F.; Dietz, H. Facile and Scalable Preparation of Pure and Dense DNA Origami Solutions. *Angew. Chem., Int. Ed.* **2014**, *53* (47), 12735−12740.
(55) Yokosuka, T.; Takamatsu, M.; Kobayashi-Imanishi, W.; Hashimoto-Tane, A.; Azuma, M.; Saito, T. Programmed Cell Death 1 Forms Negative Costimulatory Microclusters That Directly Inhibit T Cell Receptor Signaling by Recruiting Phosphatase SHP2. *J. Exp. Med.* **2012**, *209* (6), 1201−1217.
(56) Hui, E.; Cheung, J.; Zhu, J.; Su, X.; Taylor, M. J.; Wallweber, H. A.; Sasmal, D. K.; Huang, J.; Kim, J. M.; Mellman, I.; Vale, R. D. T Cell Costimulatory Receptor CD28 Is a Primary Target for PD-1-Mediated Inhibition. *Science* **2017**, *355* (6332), 1428−1433.
(57) Chen, Y.-J.; Groves, B.; Muscat, R. A.; Seelig, G. DNA Nanotechnology from the Test Tube to the Cell. *Nat. Nanotechnol.* **2015**, *10* (9), 748−760.
(58) Balakrishnan, D.; Wilkens, G. D.; Heddle, J. G. Delivering DNA Origami to Cells. *Nanomedicine* **2019**, *14* (7), 911−925.
(59) Liu, S.; Jiang, Q.; Zhao, X.; Zhao, R.; Wang, Y.; Wang, Y.; Liu, J.; Shang, Y.; Zhao, S.; Wu, T.; Zhang, Y.; Nie, G.; Ding, B. A DNA Nanodevice-Based Vaccine for Cancer Immunotherapy. *Nat. Mater.* **2021**, *20*, 421.
(60) Yuan, H.; Jiang, W.; von Roemeling, C. A.; Qie, Y.; Liu, X.; Chen, Y.; Wang, Y.; Wharen, R. E.; Yun, K.; Bu, G.; Knutson, K. L.; Kim, B. Y. S. Multivalent Bi-Specific Nanobioconjugate Engager for Targeted Cancer Immunotherapy. *Nat. Nanotechnol.* **2017**, *12* (8), 763−769.
(61) Tietjen, G. T.; Bracaglia, L. G.; Saltzman, W. M.; Pober, J. S. Focus on Fundamentals: Achieving Effective Nanoparticle Targeting. *Trends Mol. Med.* **2018**, *24* (7), 598−606.
(62) Cremers, G. A. O.; Rosier, B. J. H. M.; Riera Brillas, R.; Albertazzi, L.; de Greef, T. F. A. Efficient Small-Scale Conjugation of DNA to Primary Antibodies for Multiplexed Cellular Targeting. *Bioconjugate Chem.* **2019**, *30* (9), 2384−2392.
(63) Kick, B.; Praetorius, F.; Dietz, H.; Weuster-Botz, D. Efficient Production of Single-Stranded Phage DNA as Scaffolds for DNA Origami. *Nano Lett.* **2015**, *15* (7), 4672−4676.
(64) Bellot, G.; McClintock, M. A.; Lin, C.; Shih, W. M. Recovery of Intact DNA Nanostructures after Agarose Gel-Based Separation. *Nat. Methods* **2011**, *8* (3), 192−194.
(65) Bell, J. M.; Chen, M.; Baldwin, P. R.; Ludtke, S. J. High Resolution Single Particle Refinement in EMAN2.1. *Methods* **2016**, *100*, 25−34.

https://doi.org/10.1021/jacs.1c02298
J. Am. Chem. Soc. 2021, 143, 10131−10142